Two-dimensional femtosecond stimulated Raman spectroscopy for molecular polaritons: Dark states and beyond

Jianhua Ren [1] and Zhedong Zhang [1,2,*]

[1]*Department of Physics, City University of Hong Kong, Kowloon, Hong Kong SAR*

[2]*City University of Hong Kong, Shenzhen Research Institute, Shenzhen, Guangdong 518057, China*

(Received 28 September 2023; revised 24 April 2024; accepted 25 April 2024; published 21 May 2024)

We propose a scheme based on femtosecond stimulated Raman spectroscopy (FSRS) for N molecules in an optical cavity. With theoretical simulations, the scheme can access the collective dynamics of molecular polaritons and their coupling to vibrations, along with crosstalk between polariton and dark states. Through multidimensional projections of the FSRS signal, we identify clear signatures of the dark states, e.g., pathways and timescales that used to be invisible with resonant techniques. A microscopic theory is developed for the polaritonic FSRS, which reveals the interplay between polaritonic population and coherence dynamics. The resulting signal makes the dark states visible, thereby providing a technique for probing the dynamics of dark states and their correlation with polariton modes.

DOI: 10.1103/PhysRevA.109.053719

I. INTRODUCTION

The strong interactions between photons and molecules in microcavities lead to hybrid phases of matter, forming a superposition of molecular states and photons [1]. These excitations, known as molecular polaritons, may exhibit properties distinctly different from those of normal molecules, such as controllable many-body couplings and cooperative light emission. The complexity of molecules, arising from their various degrees of freedom, leads to rich, multiscale interactions among the excitations. A variety of intriguing phenomena have been reported in recent studies, including polariton lasing [2] and condensation [3,4], cavity-altered chemical reactivity [5–11], and topological effects [12]. All these works highlight the importance of polariton dynamics, but this remains elusive.

The strong coupling of molecules to cavities has led to extensive studies with intense debates arising from the dark states. In spectroscopy, dark states are hard to be visualized, for instance, in the absorption and fluorescence spectrum. Nevertheless, the nonradiative processes the channels causing symmetry breaking but absent in the atomic ensembles may lead to energy or information leakage from polariton states. Much theoretical and experimental effort has been devoted to the relaxation of polariton modes, where the dark states serve as exciton reservoirs for the optical systems. Notably, the crosstalk between molecular polaritons and pure molecular modes was observed in recent experiments [13,14]. A selective dynamics of dark-state polaritons coupled to bright polaritons was therefore demonstrated. Owing to their coherent and invisible nature, the dark-state polaritons exhibit dephasing, presumably crucial for the energy transfer process [15]. Moreover, the high mode density may make the dark states a promising strategy for controlling chemical reactivity and achieving the phase transition towards polariton condensation [16,17], which are still open issues. Elaborate experiments have demonstrated unusual dynamics of molecular polaritons beyond the Tavis-Cummings model, particularly when considering molecules in the condensed phase [18,19]. In the presence of solvent-induced disorder, extensive studies have shown the spectral lines to be a signature of the pure molecular states weakly coupled to cavity photons [20,21]. This indicates a localization nature. All these findings call for a comprehensive understanding of polariton dynamics in conjunction with the dark states in molecules. The scheme of two-dimensional (2D) femtosecond stimulated Raman scattering (2D FSRS) proposed in this paper leverages the off-resonant spectroscopy, leading to a real-time monitoring of the dark polaritons. Such an off-resonant technique is associated with neat interpretation and understanding for both the theory and experiments, due to the elimination of the resonant processes. This makes the 2D FSRS a promising technique to be straightforward and controllable.

In this article, we propose an off-resonant spectroscopic probe for molecular polaritons based on stimulated Raman scattering, as illustrated in Fig. 1. A 2D femtosecond stimulated Raman spectra (2D FSRS) approach is proposed for molecules strongly interacting with microcavities. Two time-delayed resonant pump fields are used for populating the electronically excited states of the molecule-cavity hybrid system. A combined narrow-band pulse ε_2 and broad-band pulse ε_3 is off-resonantly interacting with the system—after a time delay relative to the second resonant pump field—so as to induce the stimulated Raman scattering via the virtual states (e.g., the near-edge states when using UV pulses), as illustrated in Fig. 2. The FSRS signal is therefore collected along the direction of the broadband pulse ε_3. It turns out that the dark-state polaritons exhibit a prominent Raman response. Our results demonstrate a multidimensional projection of the

*zzhan26@cityu.edu.hk

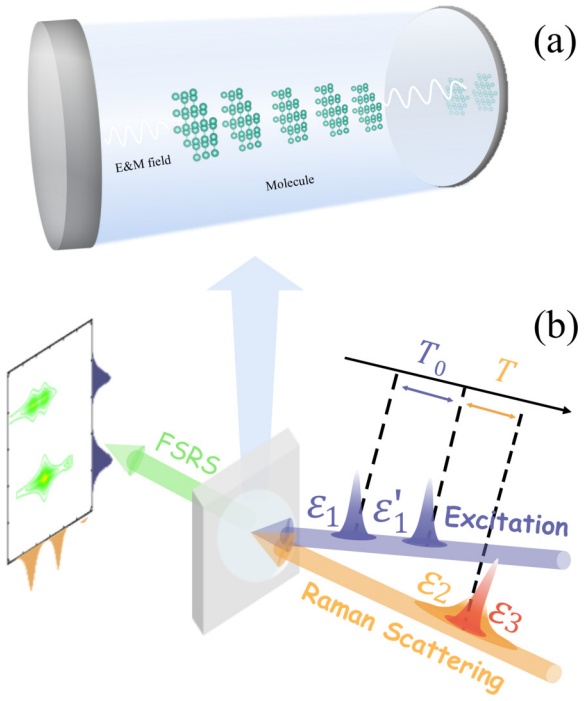

FIG. 1. (a) The microscopic structure of polaritons: Electromagnetic waves interact strongly with molecular excitations in the optical cavity, resulting in hybrid modes that manifest as quasiparticles. (b) Schematic illustration of the FSRS setup: The pump pulses $\mathcal{E}_1$ and $\mathcal{E}_1'$ are used to excite the system, after which subsequent pulses scatter through and generate the stimulated Raman transitions.

coherent FSRS signal for real-time monitoring of the dark-state dynamics. Furthermore, a microscopic polariton model is developed for the 2D FSRS, elaborating on the multiple timescale nature of the population dynamics of polaritons in crosstalk with the dark states.

The rest of the paper is organized as follows. In Sec. II we discuss the dynamics of the model used to describe the interactions between photons and molecules. Section III provides a brief introduction of FSRS. In Sec. IV we derive and numerically present the one-dimensional time-resolved FSRS signal for the molecular-polariton model. Section V presents the 2D-FSRS scheme for the molecular-polariton model. We propose a resolution procedure to monitor the real-time dynamics of the polaritons and dark polariton states. In Sec. VI we further study the charge transfer state using the 2D FSRS. Section VII presents our conclusions and remarks.

II. MODEL FOR MOLECULAR EXCITONS

A. Polariton and dark state

We consider a generic model consisting of N molecules in a single-mode optical cavity, as depicted in Fig. 1(a). Each molecule has one exciton mode, which describes the electronic excitations. The excitons essentially interact with the vibrations, which may feature a dense distribution in complex molecules. This system can be described by a model Hamiltonian $H = H_0 + H_{\rm vib} + V_{\rm int}$, where H_0 is the exciton-photon component

$$H_0 = \sum_{j=1}^{N}\left[\omega b_j^\dagger b_j + g(b_j^\dagger a + b_j a^\dagger) + \frac{\mathcal{U}}{2} b_j^\dagger b_j^\dagger b_j b_j\right] + v a^\dagger a, \tag{1}$$

where b_j and $b_j^\dagger$ are the respective annihilation and creation operators for excitons in the jth molecule, satisfying $[b_i, b_j^\dagger] = \delta_{ij}$. The operators a and $a^\dagger$ denote the annihilation and creation operators for photon modes, with $[a, a^\dagger] = 1$. We use atomic units with $\hbar = 1$ hereafter. The symbols ω and v represent the energy of the single mode for the molecule and the cavity, respectively. The photon-molecule coupling is denoted by $g = -\sqrt{2\pi v/V}\,p$, where V is the cavity volume and p is the dipole moment of the molecule. The parameter $\mathcal{U} = \sum_{a,b}\langle j_a, j_b|(\vec{d}_a\cdot\vec{d}_b - 3(\hat{n}\cdot\vec{d}_a)(\hat{n}\cdot\vec{d}_b))/4\pi\epsilon_0 R^3|j_a, j_b\rangle$ measures the interaction strength between excitons, where $\vec{d}_i = e\vec{r}_i$ are the exciton dipole moments in one molecule and $|j_a\rangle$ represents the exciton state a in the jth molecule. R is the separation between the dipoles, and $\hat{n} = \vec{R}/R$ is the unit vector in the direction from one dipole to another [22]. One observes that the total number of excitations, i.e., $M = \sum_{j=1}^{N} b_j^\dagger b_j + a^\dagger a$, is conserved due to $[M, H_0] = 0$. The Hamiltonian in Eq. (1) is thus of a block-diagonal form. This leads to a superposition subject to a certain M, forming molecule-cavity states. In the absence of $\mathcal{U}$, two modes called upper polariton (UP) and lower polariton (LP) are found, along with the other $N-1$ dark states (DSs) or the so-called dark-state polaritons (DSPs). A schematic diagram for the energy structure is demonstrated in Fig. 2, where we denote the energy of UP, LP, and DSPs as $\omega_{\rm up}$, $\omega_{\rm lp}$, and $\omega_{\rm ds}$, respectively, in addition to the trivial ground state $\omega_{\rm g}$.

The coupling of excitons to vibrational modes is of the form [23]

$$V_{\rm int} = \sum_{i}^{N}\sum_{k}\omega_{{\rm vib},k}^{i} q_{i,k} d_{i,k} b_i^\dagger b_i \tag{2}$$

with the free Hamiltonian of vibrational modes

$$H_{\rm vib} = \sum_{k}\sum_{i}^{N}\frac{1}{2}\omega_{{\rm vib},k}^{i} C_{ik}^\dagger C_{ik}. \tag{3}$$

The vibrational modes are assumed to have a dense distribution that can be described by a smooth spectral density. Here $q_{i,k} = \sqrt{1/2m\omega_{{\rm vib},k}^{i}}(C_{i,k}^\dagger + C_{i,k})$ denotes the coordinates of the molecular stretching. We define the polariton operators as follows:

$$\eta_n = \sum_{j}^{N} U_{n,j} b_j + U_{n,N+1} a. \tag{4}$$

This definition can be obtained by first excluding the $\mathcal{U}$ term and then diagonalizing the Hamiltonian H_0. The diagonalization process yields the commutation relation $[\eta_n, \eta_m^\dagger] = \delta_{nm}$. Consequently, we can reformulate the Hamiltonian in the

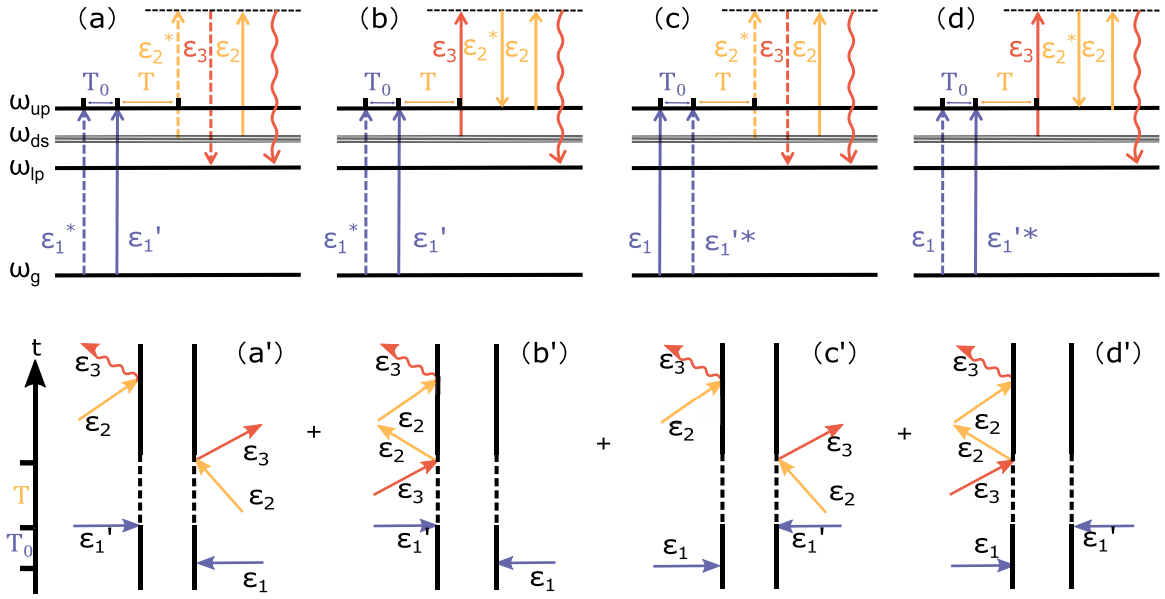

FIG. 2. (Top row) An illustration of the energy levels of molecular polaritons is provided, including the upper polariton $\omega_{\rm up}$, dark state $\omega_{\rm ds}$, lower polariton $\omega_{\rm lp}$, and ground state $\omega_{\rm g}$. The solid arrows denote the transitions of the ket states (corresponding to the left leg in the Feynman diagrams), whereas the dashed arrows denote the transitions of the bra states (corresponding to the right leg in the Feynman diagrams). The wavy arrow represents the signal. The FSRS process can be illustrated as follows: ε_1 pumps the system from the ground state to the polariton states (vertical blue arrows), which undergo a dynamics and then interact with the pulses ε_2 (narrow-band) and ε_3 (broadband) that generate the Raman scattering (yellow and red arrows). The signal is collected from the transmission of the ε_3 field. (Bottom row) Four double-side Feynman diagrams for the 2D FSRS, in a correspondence to the level diagrams in the top row. The signal is collected along the direction of the ε_3, i.e., spectral transmission of the ε_3 blue shifted with respect to the Raman probe pulse ε_2.

following form:

$$H_0 = \sum_{i=1}^{N+1} \omega_i \eta_i^\dagger \eta_i + \frac{\mathcal{U}}{2} \sum_{k,l,m,n}^{N+1} K_{klmn} \eta_k^\dagger \eta_l^\dagger \eta_m \eta_n, \tag{5a}$$

$$V_{\rm int} = \sum_{m>n,i,k}^{N+1} \mathcal{V}_{i,k} (U_{im}^\dagger U_{ni} \eta_m^\dagger \eta_n C_{i,k} + \text{H.c.}), \tag{5b}$$

where $\omega_{N+1/N} = \omega_{\rm up/lp} = \frac{1}{2}(v \pm \sqrt{4g^2 + (v-\omega)^2} + \omega)$, $\omega_{1,2,\ldots,N-1} = \omega_{ds} = \omega$, $K_{klmn} = \sum_j^N U_{jk}^\dagger U_{jl}^\dagger U_{mj} U_{nj}$, $\mathcal{V}_{i,k} = \sqrt{1/2}\omega_{{\rm vib},k}^i d_{i,k}$. Note that we have not included terms such as $\eta_m^\dagger \eta_n C_{i,k}^\dagger$ because they are negligible according to the rotating wave approximation.

From several experimental studies, the absorption and fluorescence spectra of aggregated molecular ensembles show a dense distribution of states attached to the electronic excitations, yielding inhomogeneous spectral-line broadening that results from a smooth spectral density of the vibrations [24,25]. This indicates a significant contribution from a large number of vibrational modes over a wide spectrum. To this end, we can treat the vibrations as a bath system that affects the molecule-photon system with negligible backreactions. Therefore, we consider the molecule-photon cavity system as an open system by tracing out the vibrations and obtain the polariton Redfield equation $\dot{\rho} = -i[H_0, \rho] + \hat{\mathcal{W}}\rho$ [26]

$$\hat{\mathcal{W}}\rho = \sum_{m>n} \frac{\gamma_{mn}}{2} [(\eta_m^\dagger \eta_n \rho \eta_n^\dagger \eta_m - \eta_n^\dagger \eta_m \eta_m^\dagger \eta_n \rho) \bar{n}_{\omega_{mn}} + (\eta_n^\dagger \eta_m \rho \eta_m^\dagger \eta_n - \eta_m^\dagger \eta_n \eta_n^\dagger \eta_m \rho)(\bar{n}_{\omega_{mn}} + 1)] + \text{H.c.}, \tag{6a}$$

where we have $\gamma_{mn} = \sum_i^N J_i(\omega_{mn}) U_{mi}^* U_{mi} U_{ni} U_{ni}^*$ and the spectral density [27]

$$J_i(\omega_{mn}) = 2\lambda_0 \frac{\omega \gamma_0}{\omega^2 + \gamma_0^2}. \tag{7}$$

The solution to the polariton Redfield equation is given by

$$\rho_{e_4 e_3}(t) = \sum_{e_2 e_1} \mathrm{G}_{e_4 e_3, e_2 e_1}(t) \rho_{e_2 e_1}(0), \tag{8}$$

where $G(t)$ is the Green's propagator for the Redfield equation in the absence of external fields. The polariton dynamics governed by Eq. (8) will be imprinted into the Raman response when interacting with laser pulses. Consequently, the nonlinear optical signals are capable of reading out the polariton resonance and dynamics.

III. PRELIMINARY ON FSRS

In this work our strategy involves applying stimulated Raman techniques to study femtosecond stimulated Raman spectroscopy (FSRS) for molecular polaritons and optically dark states [28–36]. The conventional FSRS takes advantages over time-resolved Raman spectroscopy, e.g., the CARS scheme, which is normally bottlenecked by the temporal and spectral scales. The FSRS can achieve the time and frequency scales subject to independent pulse parameters [33].

In 2D FSRS the excitations of the system are created by resonant pump pulses; then a pair of overlapped broad-band and narrow-band pulses scatter off the system, thereby producing the stimulated Raman transition. The interaction thus

reads

$$H_{\rm int} = \alpha\varepsilon_2^\dagger(t)\varepsilon_3(t) - \mu\varepsilon_1^\dagger(t) + \text{H.c.}, \tag{9}$$

where μ represents the electric dipole operator, and α denotes the Raman polarizability operator, i.e., $\alpha = \sum_{e,e'} \alpha_{ee'}|e\rangle\langle e'|$ [37]:

$$\alpha_{ee'} = \sum_i^N P_i^2 |U_{ie}^\dagger U_{e'i}| \left(\frac{1}{\omega_i - \omega_{e'}} + \frac{1}{\omega_i - \omega_e} \right). \tag{10}$$

The energy of the near-edge states $|r_i\rangle$ is high enough to ensure that it does not admit any interactions with the cavity [38], and P_i refers to the transition dipole between different energy levels in the ith molecule, namely, $P_i = \langle e_i|\mu|r_i\rangle$. Since $|r_j\rangle$ is highly excited and thus is decoupled from the cavity, a random phase is essentially attached to the Raman transition amplitude, i.e., $U_{ei} = |U_{ei}|e^{i\phi_{ei}}$. Therefore, we have to take the ensemble average over the phase $\langle |U_{ie}^\dagger U_{e'i}| e^{i(\phi_{e'i} - \phi_{ei})} \rangle_{\rm ave} = |U_{ie}^\dagger U_{e'i}|$, ensuring that the Raman polarizability between two excited states is well defined.

The transmission of the Raman probe (short pulse) is measured so that the optical signal is $S = \langle \varepsilon_3^*(\omega)\varepsilon_3(\omega)\rangle$. Using Heisenberg's equation of motion for the fields, one has [39] $S = -i\int dt \langle [\varepsilon_3^\dagger(\omega)\varepsilon_3(\omega), H_{\rm int}]\rangle$. Here the most significant terms remain, namely, the time-ordered resonant pump and Raman probe. As the Raman pulses excite the molecules, polariton modes then begin to interact with both dark states and the vibrational bath. This interaction causes relaxation and repopulation, and the relevant dynamical information is encoded in the density matrix described by the Born-Redfield equation [26]. As a result, the multidimensional projections of the FSRS signal reflect the real-time information regarding the dark states and their correlations with polariton modes. Some algebra gives the FSRS signal [39]

$$S(\omega, T) \propto \frac{1}{\pi} \text{Im} \int_{-\infty}^{+\infty} dt\, e^{i\omega(t-T)} \varepsilon_3^*(\omega)\varepsilon_2(t-T)\, \text{Tr}(\hat{\alpha}\rho). \tag{11}$$

One has to calculate the density matrix ρ up to the third order of $H_{\rm int}$ so as to have the FSRS [40].

IV. ONE-DIMENSIONAL FEMTOSECOND STIMULATED RAMAN SPECTROSCOPY

To calculate the FSRS signal from Eq. (11), we must perform the integral over the time domain. While this is generally challenging, it can be achieved by assuming a Lorentzian spectral profile

$$\varepsilon_i(t - T_i) = \theta(t - T_i) e^{-\frac{t-T_i}{\sigma_i}} e^{-i\omega_i t}, \tag{12}$$

where T_i and ω_i denote the central time and frequency of the pulse, respectively. The resonant pump ε_1 excites the system, while the pulses ε_2 and ε_3 act with a time delay $T = T_2 - T_1$ relative to ε_1, thereby inducing the Raman transition. The pulse fields inducing the Raman transition have identical arrival times, i.e., $T_2 = T_3$. Due to the broadband nature of the resonant pump, a wide spectrum of excited states is covered. The FSRS signal, as given by Eq. (11), thus includes the population components ρ_{ee} and the coherence components $\rho_{ee'}$ $(e \neq e')$ of molecular polaritons.

When the Raman fields and the pump field are well separated in time, namely, when $T \gg \sigma_1, \sigma_2, \sigma_3$, the FSRS spectroscopic experiment can be viewed as a three-step process: preparation, propagation, and Raman detection. The two resonant pump fields create an initial doorway state for the polaritons, which then propagates and is finally probed at a time delay T using a window operation. For a precise definition of this three-step process, we expand Eq. (11) in terms of the Raman coupling, resulting in

$$\begin{aligned} S_{\rm 1D}(\omega - \omega_2, T) \propto N &\int_{-\infty}^{\infty} dt \int_{-\infty}^{t} d\tau e^{i(\omega-\omega_2)t} \varepsilon_3^*(\omega) \\ &\times \varepsilon_2(t-T)\varepsilon_2^*(\tau - T)\varepsilon_3(\tau - T) \\ &\times \text{Tr}\{\alpha[\alpha(\tau), \rho_0]\} \\ \approx N &\int_{-\infty}^{\infty} dt \int_{-\infty}^{T} d\tau e^{i(\omega-\omega_2)t} \varepsilon_3^*(\omega)\varepsilon_2(t)\varepsilon_2^*(\tau) \\ &\times \varepsilon_3(\tau)\text{Tr}\{\alpha(t)[\alpha(\tau), \rho(T)]\}. \end{aligned} \tag{13}$$

Here $= 1/\sqrt{N}\sum_j^N \alpha_j$ describes the total Raman polarizability of the N molecules. With a proper approximation in the last step, assuming that the delay T is longer than the pulse duration, such an approximation is effective for most ultrafast molecular spectroscopic experiments. This approach allows for the definition of the *Raman window operators*:

$$W(\omega - \omega_2) = \int_{-\infty}^{\infty} dt e^{i(\omega-\omega_2)t} \varepsilon_3^*(\omega)\varepsilon_2(t)\alpha(t), \tag{14a}$$

$$V(\sigma) = \int_{-\infty}^{T} d\tau \varepsilon_2^*(\tau)\varepsilon_3(\tau)\alpha(\tau). \tag{14b}$$

Using Eqs. (13), (14a), and (14b), the FSRS signal for the Raman shift $\omega - \omega_2$ reads

$$S_{\rm 1D}(\omega - \omega_2, T) \propto \text{Re}\,\text{Tr}\{W(\omega - \omega_2)[V(\sigma), \rho(T)]\}. \tag{15}$$

To prepare the polariton state $\rho(T)$, the *doorway operators* are helpful to describe the process by the resonant pump pulses. A *doorway-Raman-window* representation can therefore be developed and would be powerful for an unified understanding of multidimensional FSRS. We will elaborate on this in Sec. V for the 2D FSRS.

To closely observe the FSRS signal and numerically study the dynamics of polaritons and dark states, we set a strong coupling $g\sqrt{N} = 0.05\sqrt{2}$ without losing generality. It is worth noting that the parameters $\omega = 1.84$ eV and $\mathcal{U} = 0.02$ eV for simulations are taken from the cyanine dye aggregates [41]. The ultraviolet (UV) pulses are thus preferably used to generate the Raman transitions between the exciton-polariton states.

Nevertheless, real-life scenarios are even more complicated. Numerous aspects, such as phonons, impurities, collisions, noise, and cavity imperfection, can cause the dephasing and consequently affect the spectral line width. Unfortunately, one is unable to take into account all these channels at a microscopic level, for a clean and neat picture from the theory. One can therefore use a parameter γ to account for these dephasing processes at a phenomenological

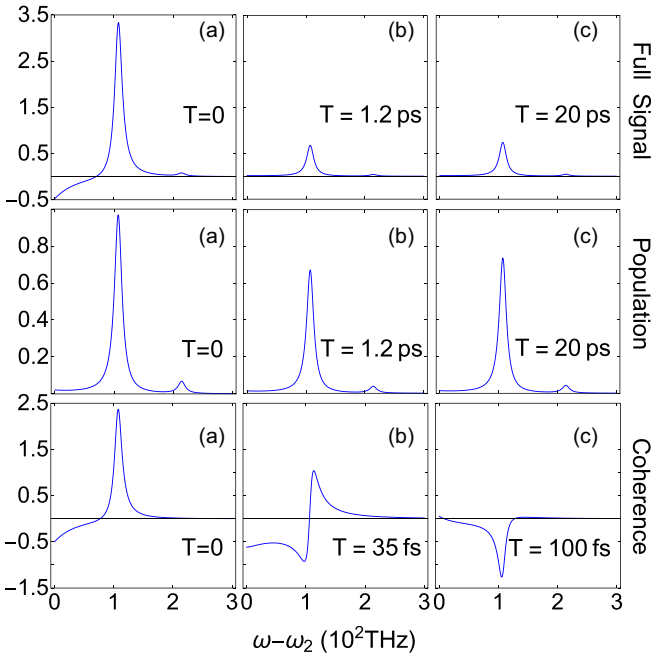

FIG. 3. FSRS signals of $N = 10$ molecules without detuning are shown. We have taken $\delta = 243$THz as the center frequency difference, $\sigma_2 = 1$ ps, and $\sigma_3 = 35$fs for the broad pulse ε_2 and the narrow pulse ε_3, respectively. To better simulate the real situation, we introduce the phenomenological parameter $\gamma = 100$THz to modify ξs by $\xi_{e_5e_3} = \omega_{e_5e_3} - i(\gamma_{e_5e_3} + \gamma)$, which can account for the possible dephasing rate caused by experimental uncertainty. Subsequent signals use the same parameters. Horizontally, panels (a), (b), and (c) monitor the real-time evolution of the FSRS signals with different time delays T. (Top row) Full signal, (middle row) population component, and (bottom row) coherence component where the full signal is a sum of the population and coherence components.

level. In other words the complex frequency becomes $\xi_{e_5e_3} = \omega_{e_5e_3} - i(\gamma_{e_5e_3} + \gamma)$. The larger γ is, the broader lines are for the FSRS signal. We present the simulated polariton FSRS signals [given by Eq. (15)] in Fig. 3 and Fig. 5 with different

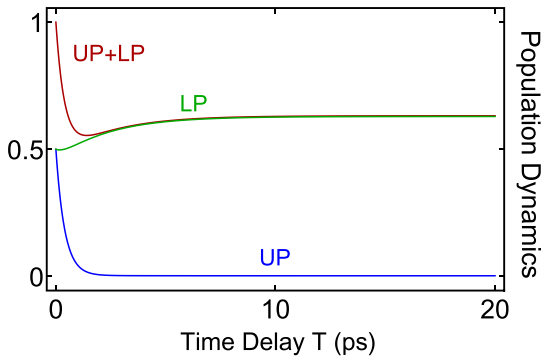

FIG. 4. Dynamics of the populations are solved using the master equation, assuming no detuning between the molecules and the cavity. In this scenario, the molecules are initially pumped into a superposition of the upper polariton and the lower polariton, with the transition dipole being $\mu_{g,up} = \mu_{g,lp}$.

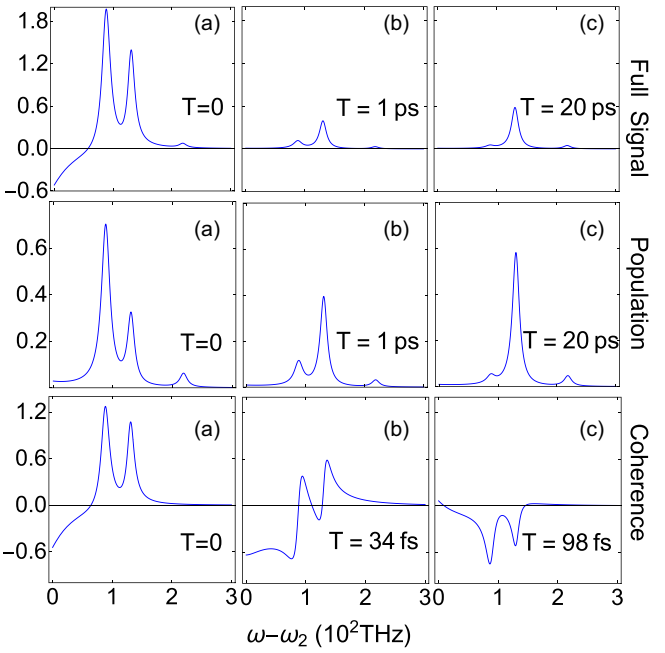

FIG. 5. FSRS signals of $N = 10$ molecules, with a detuning between the molecule and cavity of $\omega - v = 1.25g$. Panels (a), (b), and (c) display the FSRS signals at different time delays. Vertically, the total signals, populations, and coherences are displayed sequentially. The relative intensity of the peaks observed during a real-time delay can be used to resolve the populations of the molecular states.

detunings. Before moving on to the detailed analysis of the signals, let us briefly comment on the implications derived from the one-dimensional (1D) signal, without delving into many numerical details. According to first-order perturbation theory, we know that the pulse ε_1 initially excites the polaritons to the superposition state $\mathcal{N}^{-1}(\mu_{up,g}|\mathrm{UP}\rangle + \mu_{lp,g}|\mathrm{LP}\rangle)$, where $\mathcal{N} = \sqrt{\mu_{up,g}^2 + \mu_{lp,g}^2}$ is the normalization factor.

Generally speaking, the intensity of the signal curve indicates the probability of a certain process occurring, which boils down to the population of the relevant states. For example, a peak located at $\omega_{e_3e_5} \gtrless 0$ reflects that the linear combination of density matrices $\rho_{e_3,e_3} + \rho_{e_5,e_5}$ is dominating, rather than the individual populations ρ_{e_3,e_3} or ρ_{e_5,e_5}. This is attributed to the two components: dissipative [Figs. 2(a′) and 2(c′) and parametric [Figs. 2(b′) and 2(d′)] processes that give the same Raman resonance. As shown in Figs. 2(a)–2(d), where $e_3 =$ ds and $e_5 =$ lp, we observe that the peak is located at $\omega_{ds,lp}$, indicating the transition progression from (a) to (d). This argument can guide us to qualitatively decode more populations from the FSRS signal.

In the following sections, we will discuss 1D FSRS in detail for cases with or without detuning between molecules and the cavity. We will focus on the blue Raman shifts of the signal hereafter.

A. Zero cavity-molecule detuning

In this subsection, we begin by considering the case of zero detuning between the molecular excitons and the cavity, i.e.,

$\omega - v = 0$. In Fig. 3 we display the total signal, population, and coherence on the top, middle, and bottom lines, respectively. Notice that the signal may show negativity somewhere. This arises from the oscillatory nature of the quantum coherence created by the broadband pump pulse at zero time delay.

Let's begin by analyzing the population, as shown in the middle line of Fig. 3. Owing to the vanishing detuning, $\omega - v = 0$, we have $\omega_{\mathrm{up,ds}} = \omega_{\mathrm{ds,lp}}$. As a consequence, we can observe two peaks: (1) the transitions UP $\leftrightarrow$ Dark and Dark $\leftrightarrow$ LP that merge together and (2) the transition UP $\leftrightarrow$ LP. By varying the time delay T, the populations at the dark states can be resolved from the two peaks in Figs. 3(a)–3(c). However, due to the transitions UP $\leftrightarrow$ Dark and Dark $\leftrightarrow$ LP merging into one peak at 107 THz, Fig. 3 enables real-time monitoring of the coupled dynamics for the polariton states, i.e., $\rho_{\mathrm{up,up}} + \rho_{\mathrm{lp,lp}}$. The peak at 107 THz includes the trasition process from Figs. 2(a)–2(d) with the Raman shift $\omega_{\mathrm{up,ds}}, \omega_{\mathrm{ds,lp}}$. This is further confirmed by the simulations of the polariton Redfield equation in Eq. (6a), which depict the population dynamics of the polariton states in Fig. 4. Moreover, Fig. 3 also shows that the signal resolves the coherence nature of the polaritons within a short timescale. In particular, the peak at $\omega_{\mathrm{up,ds}}$ ($\omega_{\mathrm{ds,lp}}$) presents an oscillation during approximately 1 ps, on top of the population components $\rho_{\mathrm{up,up}} + \rho_{\mathrm{ds,ds}}$. This reveals the coherence between the UP and the LP.

B. With detuning $\omega - v = 1.25g$

We consider a detuning of $\omega - v = 1.25g$ between the molecular excitons and cavity photons. As observed in the energy-level structure of polaritons, the two transitions UP $\leftrightarrow$ Dark and Dark $\leftrightarrow$ LP result in a splitting of the spectral lines.

Beginning with the population analysis shown in the middle line of Fig. 5, we clearly observe three peaks at $\omega_{\mathrm{up,ds}} =$ 88THz, $\omega_{\mathrm{ds,lp}} = 130$THz, and $\omega_{\mathrm{up,lp}} = 213$THz. As in the previous analysis, the peak at $\omega_{\mathrm{up,ds}}$ is expected to represent the combined dynamics of the UP and dark states. This peak decreases with time delay, in contrast to the behavior of the LP state. The peak at $\omega_{\mathrm{ds,lp}}$, however, continually increases, aligning with the growth of the LP state. This peak corresponds to the combined dynamics of the LP and dark states. Similarly, the peak for $\omega_{\mathrm{up,lp}}$ reflects the dynamics of the UP and LP states. Its behavior is consistent with the dynamics of the superposition of UP and LP, which first decreases and then begins to increase.

The population dynamics of polaritons coupled to the dark states can be read out from the FSRS signal. For a longer timescale, longer than the coherence lifetime, the population dynamics of cavity polaritons dominate. After some manipulations, we are able to find a group of algebraic equations for populations and signals under the impulsive approximation, with only small errors:

$$
\begin{aligned}
S_{\mathrm{1D}}^{(p)}(\omega_{\mathrm{up}} - \omega_{\mathrm{ds}}, T) &\simeq \tilde{\alpha}_{\mathrm{1D,upds}}^{(1)}[\rho_{\mathrm{dsds}}(T) + \rho_{\mathrm{upup}}(T)] + \tilde{\alpha}_{\mathrm{1D,dslp}}^{(1)}[\rho_{\mathrm{dsds}}(T) + \rho_{\mathrm{lplp}}(T)] + \tilde{\alpha}_{\mathrm{1D,uplp}}^{(1)}[\rho_{\mathrm{lplp}}(T) + \rho_{\mathrm{upup}}(T)],\\
S_{\mathrm{1D}}^{(p)}(\omega_{\mathrm{ds}} - \omega_{\mathrm{lp}}, T) &\simeq \tilde{\alpha}_{\mathrm{1D,upds}}^{(2)}[\rho_{\mathrm{dsds}}(T) + \rho_{\mathrm{upup}}(T)] + \tilde{\alpha}_{\mathrm{1D,dslp}}^{(2)}[\rho_{\mathrm{dsds}}(T) + \rho_{\mathrm{lplp}}(T)] + \tilde{\alpha}_{\mathrm{1D,uplp}}^{(2)}[\rho_{\mathrm{lplp}}(T) + \rho_{\mathrm{upup}}(T)],\\
S_{\mathrm{1D}}^{(p)}(\omega_{\mathrm{up}} - \omega_{\mathrm{lp}}, T) &\simeq \tilde{\alpha}_{\mathrm{1D,upds}}^{(3)}[\rho_{\mathrm{dsds}}(T) + \rho_{\mathrm{upup}}(T)] + \tilde{\alpha}_{\mathrm{1D,dslp}}^{(3)}[\rho_{\mathrm{dsds}}(T) + \rho_{lplp}(T)] + \tilde{\alpha}_{\mathrm{1D,uplp}}^{(3)}[\rho_{\mathrm{lplp}}(T) + \rho_{\mathrm{upup}}(T)]
\end{aligned}
\tag{16}
$$

where the coefficients are defined by

$$\tilde{\alpha}_{\mathrm{1D},ab}^{(j)} = \frac{1}{\pi}\mathrm{Im}(-i)^3 \sum_{n}^{N-1} |\alpha_{a,b}|^2 f(\omega^{(j)}, \xi_{ab}).$$

Here we define the function $f(v, \xi)$ to simplify the final expressions. This function is related only to the pulse parameter and the energy gap and is derived from the integral of (15):

$$f(v,\xi) = \frac{1}{-\frac{1}{\sigma_2}+i\delta-\frac{1}{\sigma_3}+i\xi}\left(\frac{1}{i(v-\xi)-\frac{1}{\sigma_2}} - \frac{1}{-\frac{2}{\sigma_2}+i(v+\delta)-\frac{1}{\sigma_3}}\right), \tag{17}$$

where we assume that the broadband Raman pulse ε_3 has a duration much shorter than the polariton relaxation and dephasing processes. In these formulas, $j = 1, 2, 3$ indicates that $\omega^{(1,2,3)}$ corresponds to $\omega_{\mathrm{up,ds}}, \omega_{\mathrm{ds,lp}}, \omega_{\mathrm{up,lp}}$ respectively, and $\delta = \omega_2 - \omega_3$. Using (16), we can solve for the density matrices $\rho_{\mathrm{ds,ds}}$, $\rho_{\mathrm{up,up}}$, and $\rho_{\mathrm{lp,lp}}$ in terms of the FSRS lines, given the superposition $\mathcal{N}^{-1}(\mu_{\mathrm{up,g}}|\mathrm{UP}\rangle + \mu_{\mathrm{lp,g}}|\mathrm{LP}\rangle)$ as an initial state. We illustrate the dynamics of this picture in Fig. 6, where the initial state is a superposition of LP and UP states with $\mu_{\mathrm{up,g}} = 2.443$, $\mu_{\mathrm{lp,g}} = 2.008$, and the normalization is given by $\mathcal{N} \simeq 3.162$. Due to the existing detuning between molecules and the cavity, the transition dipole between UP and LP is no longer equal, which explains why UP and LP states have different initial weights in Fig. 6. As displayed in Fig. 6, the bright and dark polariton populations resolved by Eq. (16) with the FSRS signal perfectly match those obtained from the Redfield equation Eq. (6a). Interestingly, after relaxation ends around $T = 20$ ps, dark-state polaritons occupy a significant

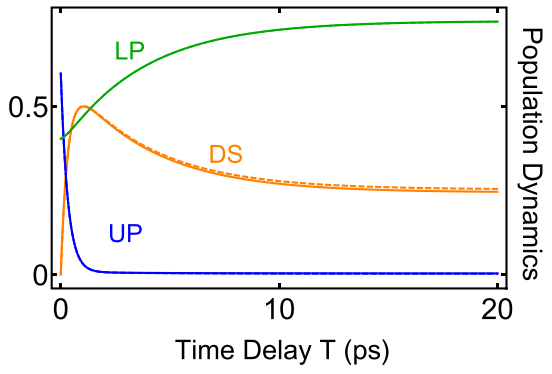

FIG. 6. Comparison between the populations resolved by the FSRS signal (dashed line) and the populations obtained from the master equation (solid line), with a detuning of $1.25g$. The transition dipole values are $\mu_{\mathrm{g,up}} = 2.443$ and $\mu_{\mathrm{g,lp}} = 2.008$. The green, orange, and blue colors correspond to the dynamics of the upper polariton, dark state, and lower polariton, respectively.

proportion. This insightful finding suggests that dark states can be more effectively explored after relaxation.

Although we use FSRS to accurately resolve the dynamics of the upper and lower polaritons, as well as the dark states, the main limitation is that we can only initially pump the superposition of the upper and lower polaritons, not any of them individually. To address this issue, we propose to add a second pump pulse ε_1', and use the time delay T_0 between the $\varepsilon_1 - \varepsilon_1'$ pulses to control the excitation of the polariton states, as illustrated in Sec. V.

V. TWO-DIMENSIONAL FEMTOSECOND STIMULATED RAMAN SPECTROSCOPY

To overcome the spectral bottleneck presented by the 1D FSRS above, we will use two pulses for the selective excitation of molecular polaritons. Other scenarios of 2D spectroscopy can also be found in the literature, e.g., [42–44]. Here a pair of short pulses, with an additional delay T_0, pump the system, creating resonant excitations. The Raman emission is then collected after a delay of T relative to the second pump pulse, as depicted in Fig. 1(b). Using the Dyson series up to the second order against the couplings with the resonant pump pulses, we determine the polariton density matrix

$$\begin{aligned}\rho(t) &= N\int\!\!\int_{-\infty}^{t} d\tau_2\, d\tau_1 \theta(\tau_2-\tau_1)\mu(\tau_2)\rho_0\mu(\tau_1)\\ &\quad\times \varepsilon_1(\tau_2-T_1')\varepsilon_1^*(\tau_1-T_1)+\text{H.c.}\\ &\approx N\int_{-\infty}^{\infty} dt'\int_{-t'}^{\infty} dt''\hat{G}(t-T_1')[\mu(t')\rho_0\mu(-t'')]\\ &\quad\times \varepsilon_1(t')\varepsilon_1^*(T_0-t'')+\text{H.c.},\end{aligned} \tag{18}$$

where $t \gg$ is the pulse duration. $\varepsilon_1(t-T_1)$ and $\varepsilon_1(t-T_1')$ denote the two resonant pump fields, with $T_0 \equiv T_1' - T_1$. The Green's propagator, $\hat{G}(t)$, is defined in Eq. (8) for the polariton systems. Equation (23) enables the definition of the *doorway operators* for the resonant excitation process [45]

$$\begin{aligned}D(T_0) &= N\int_{-\infty}^{\infty} dt'\int_{-t'}^{\infty} dt''\varepsilon_1(t')\varepsilon_1^*(T_0-t'')\\ &\quad\times \mu(t')\rho_0\mu(-t'')+\text{H.c.},\\ D(\omega_0) &= \int_{-\infty}^{\infty} dT_0 e^{i\omega_0 T_0} D(T_0)\end{aligned} \tag{19}$$

so that

$$\rho(t) = \hat{G}(t-T_1')D(T_0). \tag{20}$$

By inserting Eq. (20) into Eq. (15) and performing the Fourier transform over T_0, the calculations proceed as usual. Consequently, we obtain the 2D-FSRS signal in the *doorway-Raman-window* formalism,

$$\begin{aligned}&S_{\text{2D}}(\omega-\omega_2, T, \omega_0)\\ &\quad\propto \text{Im}\,\text{Tr}\{W(\omega-\omega_2)[V(\sigma), \hat{G}(T)D(\omega_0)]\};\end{aligned} \tag{21}$$

with $T \gg$ pulse durations, this means that the Raman pump-probe fields are temporally separated from the resonant pump fields. $W(\omega-\omega_2)$ and $V(\sigma)$ are the Raman window operators, as given by Eqs. (14a) and (14b), respectively. The salient

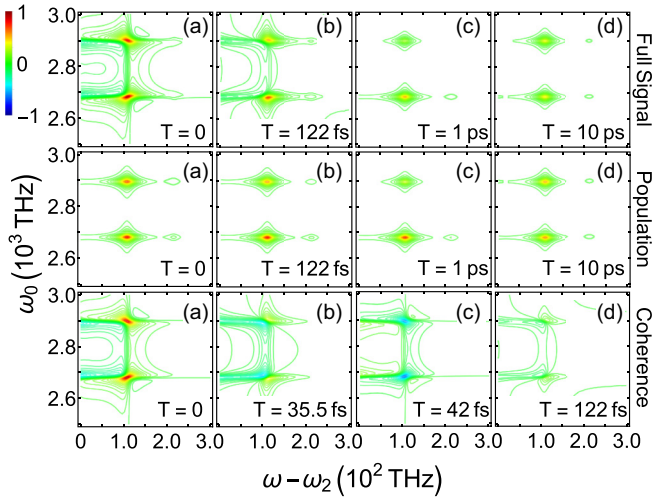

FIG. 7. Two-dimensional FSRS signal without the detuning.

feature of the 2D-FSRS signal, as seen from (21), is that it allows selective access to the polariton states via the pump. We can then expect real-time monitoring of the pathways of polariton dynamics, a task that is challenging for the 1D-FSRS signal.

Before the discussions, it is worthy of having some back-of-the-envelop analysis for the 2D-FSRS signal. From Fig. 2 and Eq. (21), one can see that each peak normally captures the four Feynman diagrams, i.e., involving both the dissipative and parametric components. In other words, each spectral resonance in the 2D signal encompasses the four transitions shown in Figs. 2(a)–2(d). Nevertheless, our strategy in what follows will enable a capability of resolving the effects from different transition configurations and the dynamics specific to each state. For the molecules with more complicated structures that may involve local impurities or charge-transfer states, a sophisticated way of directly accessing the dark states is to include the dissipative components only whereas the parametric components vanish. This will be detailed in Sec. VI.

A. Without detuning $\omega - v = 0$

Let's briefly analyze the behavior of the 2D-FSRS signal shown in Fig. 7, where $\delta = 0$. Different values of ω_0 enable the selection of different initial pumping states, as indicated by the vertical axis in Fig. 7. From this axis, it is clear that the peaks are localized around either the upper polariton (at $\omega_0 = 2890$THz) or the lower polariton (at $\omega_0 = 2680$THz), corresponding to initial pumping into the upper and lower polariton, respectively. In other words, analyzing the peaks that are vertically localized around the upper polariton will reveal the real-time populations for the initial upper pump, and similarly for the lower polariton case.

To analyze the case with initial pumping to the upper polariton, we should focus on the upper peaks in a given plot of Fig. 7. We observe that the signal is dominated by two peaks corresponding to $\omega - \omega_2 = \omega_{\text{up,ds}} = \omega_{\text{ds,lp}} = 103$THz and $\omega - \omega_2 = \omega_{\text{up,ds}} = 206$THz. Because $\omega - v = 0$, the energy gap $\omega_{\text{up,ds}}$ equals $\omega_{\text{ds,lp}}$. In this case, the first peak is the

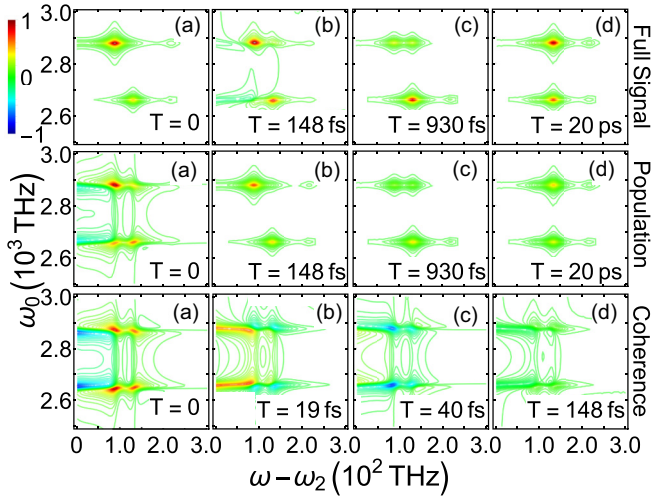

FIG. 8. Two-dimensional FSRS signal obtained with a detuning of $1.25g$.

merged one from $\omega_{up,ds}$ and $\omega_{ds,lp}$ due to zero detuning. Consequently, as in the 1D case, the peak at $\omega - \omega_2 = \omega_{up,ds} = \omega_{ds,lp}$ reflects a mixed population from the upper polariton, dark state, and lower polariton with different ratios, making it difficult to obtain valid information about each of them. However, the peak at $\omega - \omega_2 = \omega_{up,ds}$ encodes the information of only the upper and lower polariton. Its intensity first decreases and then grows, consistent with the dynamics of $\rho_{up,up} + \rho_{lp,lp}$ shown in Fig. 9(a) below. Similarly, when the initial pump is pulsed to the lower polariton (the $\omega_0 = 2680$THz line), the intensity of the peak at $\omega - \omega_2 = \omega_{up,ds}$ continues to decrease, aligning with the dynamics of $\rho_{up,up} + \rho_{lp,lp}$, as shown in Fig. 9(b).

In the coherence part of Fig. 7, we see that the peaks are concentrated vertically on the upper polariton ($\omega_0 = 2890$THz) and lower polariton ($\omega_0 = 2680$THz), implying that the coherence oscillates only between the UP and LP states. A simple explanation is that we cannot initially pump to the dark state. The oscillation and decay in the coherence section of Fig. 7 are clearly observable. The combination of population and coherence is shown on the top line in Fig. 7, where we observe that there are no coherence contributions anymore at T = 1 ps.

Until now, we have observed the dynamics of $\rho_{up,up} + \rho_{lp,lp}$. However, obtaining their individual dynamics is challenging due to the overlapping of the first two peaks,

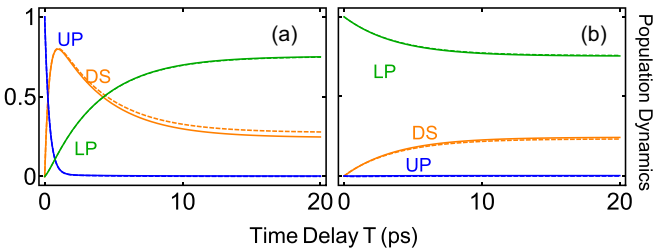

FIG. 9. Comparison between the population resolved by the signal (dashed line) and the population obtained from the master equation (solid line), for $\omega - v = 1.25g$.

$\omega - \omega_2 = \omega_{up,ds}$ and $\omega - \omega_2 = \omega_{ds,lp}$. In the following sections, we will turn on the detuning, which will separate these two peaks.

B. With detuning $\omega - v = 1.25g$

In a global view, we observe two peaks at ω_{up} and ω_{lp} when taking slices along ω_0. This is due to the destructive interference in the dark-state polaritons that results in zero net dipole. Nevertheless, three peaks can be seen along the slices with fixed ω_0. This indicates the active response of the dark-state polaritons.

The first row of Fig. 8 shows the full 2D FSRS given by Eq. (21), with scanning the delay T. For the slice at $\omega_0 = \omega_{up} = 2890$THz, Fig. 8(a) depicts that the signal is dominated by two peaks at $\omega_{up,ds} = 88$THz and $\omega_{up,lp} = 218$THz. This means the population of the system is at the upper polariton state. When the delay T varies, we see the energy transfer from UP to DSPs, evident by the increase of the peak at $\omega - \omega_2 = \omega_{ds,lp}$ in Figs. 8(b) and 8(c). After a longer delay, as seen from Fig. 8(d), the DSPs are densely populated, whereas the population at the LP state is less. This is attributed to the large number of DSPs.

Figures 8(a)–8(d) further show different timescales associated with different pathways. In particular, the peak at ($\omega - \omega_2 = \omega_{ds,lp}$, $\omega_0 = \omega_{up}$) shows a fast increase within 930 fs, dramatically different from the one at ($\omega - \omega_2 = \omega_{up,lp}$, $\omega_0 = \omega_{up}$) that shows a considerable change within 20 ps. We thus observe a faster energy transfer from UP to DSPs than from UP to LP. This can be understood neatly by the large density of the DSPs, much higher than the bright polariton states revealed in resonant spectroscopic experiments. The transition rate is $2\pi|\langle DS|V_{int}|UP\rangle|^2\rho(E_{ds})$ from Fermi's Golden Rule, which is enhanced by the mode density of the states. When slicing Figs. 8(a)–8(d) at $\omega_0 = \omega_{lp}$, we see the dynamics when initially pumping to the LP state. The results present a dramatic difference from those with $\omega_0 = \omega_{up}$, resulting in a slightly more subtle analysis due to the resolution issue for the figures. Nonetheless, we can still find the peak around $\omega_{ds,lp}$ barely varying with the delay, while the spectral line gets broadened slightly towards the peak at $\omega_{up,ds}$. The peak at $\omega - \omega_2 = \omega_{up,lp}$ shows low intensity, indicating a weak population at the UP state.

Notably, from the comparison between the top and middle rows of Fig. 8, it is evident that the DSPs can be greatly populated when the system is pumped to the UP state rather than the LP state. This indicates energy harvesting by the DSPs, which is important for understanding the kinetic and thermodynamic properties of molecules in cavities. As an optical signal, Fig. 8 clearly demonstrates real-time monitoring of the DSPs coupled to other molecular states, illustrating the crucial role of the DSPs.

Within a shorter timescale, the 2D FSRS reveals the coherence effect in the cavity-polariton systems, evidenced by the fast oscillations. By carefully checking the oscillating frequency, as supported by Fig. 8 (third row), the quantum coherence between UP and LP states is captured. This is due to the broadband nature of the pump fields that create a coherent superposition of $a|UP\rangle + b|LP\rangle$. Such polaritonic coherence is resolved by the FSRS signal over a short timescale,

whereas the FSRS signal is dominated by the polariton populations over longer timescales. The polariton dynamics can be monitored in a more advanced way through a sophisticated method, namely, by understanding the intrinsic connection of peak intensities to the populations that dominate over longer timescales. Consequently, a group of algebraic equations can be found:

$$S_{2D}^{(p)}(\omega_{up}-\omega_{ds},\omega_{up},T)\simeq\tilde{\alpha}_{up,ds}^{(1)}[\rho_{dsds}(T)+\rho_{upup}(T)]+\tilde{\alpha}_{ds,lp}^{(1)}[\rho_{dsds}(T)+\rho_{lplp}(T)]+\tilde{\alpha}_{up,lp}^{(1)}[\rho_{lplp}(T)+\rho_{upup}(T)],$$
$$S_{2D}^{(p)}(\omega_{ds}-\omega_{lp},\omega_{up},T)\simeq\tilde{\alpha}_{up,ds}^{(2)}[\rho_{dsds}(T)+\rho_{upup}(T)]+\tilde{\alpha}_{ds,lp}^{(2)}[\rho_{dsds}(T)+\rho_{lplp}(T)]+\tilde{\alpha}_{up,lp}^{(2)}[\rho_{lplp}(T)+\rho_{upup}(T)],$$
$$S_{2D}^{(p)}(\omega_{up}-\omega_{lp},\omega_{up},T)\simeq\tilde{\alpha}_{up,ds}^{(3)}[\rho_{dsds}(T)+\rho_{upup}(T)]+\tilde{\alpha}_{ds,lp}^{(3)}[\rho_{dsds}(T)+\rho_{lplp}(T)]+\tilde{\alpha}_{up,lp}^{(3)}[\rho_{lplp}(T)+\rho_{upup}(T)], \quad (22)$$

where the coefficients are defined by

$$\tilde{\alpha}_{a,b}^{(j)}=\frac{1}{\pi}\mathrm{Im}(-i)^3\sum_{n}^{N-1}|\alpha_{a,b}|^2|\mu_{g,up}|^2 \times\left(\frac{1}{i\gamma_{gup}}+\frac{1}{i\gamma_{upg}}\right)f(\omega^{(j)},\xi_{ab}). \quad (23)$$

We can solve the density matrices using (22) in both cases, i.e., when pumping to the upper and lower polariton. The resolved population turns out to match perfectly with the real dynamics governed by the master equation (see Fig. 9).

C. With detuning $\omega - v = -1.25g$

We can also consider the negative detuning, such as $\omega - v = -1.25g$. In this case $\omega_{up,lp}$ is the same as in the previous case (i.e., $\omega - v = 1.25g$); however, the energy gaps of $\omega_{up,ds}$ and $\omega_{ds,lp}$ have been exchanged. Similarly, we show the full signal, population, and coherence in Fig. 10.

It is immediately evident from Fig. 10 that the trends for the peaks do not deviate significantly from the positive detuning case, indicating similar behavior for the populations, which we do not need to discuss further. However, the specific details of the dynamics indeed change. We demonstrate these changes in the resolved dynamics and the real dynamics in Fig. 11, which, of course, fit well. The most significant discrepancy with the positive detuning is a substantial increase in the percentage of the dark state in the populations. This occurs because dark states with negative detuning have lower energy compared to the positive detuning case, making the dark states more easily "accessible." Therefore, to prevent the dark state from becoming scarce, we could consider setting the detuning to a negative value.

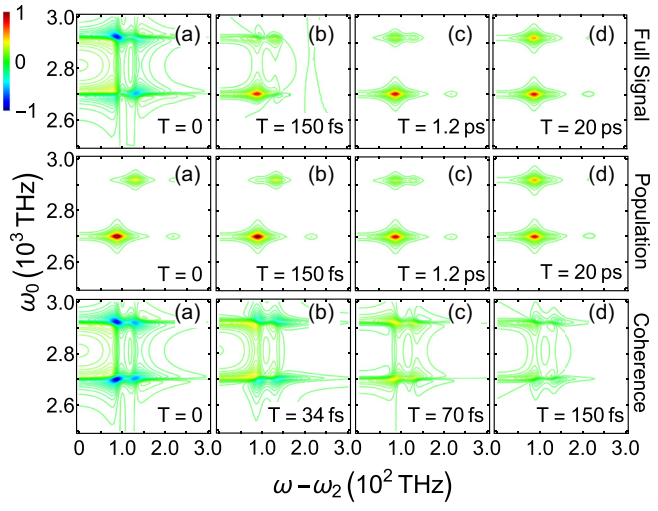

FIG. 10. Two-dimensional FSRS signal with the detuning of $\omega - v = -1.25g$.

VI. 2D FSRS WITH CHARGE TRANSFER STATES

There are molecules reactive for electron transfer, accessing the charge transfer states (CTs). The CTs typically have energies lower than the first excited states of the molecules [46]. Our strategy is essentially to induce the stimulated Raman transition that ends up at the CTs. As the CTs are difficult to excite directly by the pumping pulse, the FSRS signal for the molecular polaritons can be cleaner than before. This is evidenced by the fact that only the components (a′) and (c′) in the Feynman diagrams (Fig. 2) survive. Assuming the near-edge states can be radiatively coupled to both the molecular excitons and the CTs, the Raman polarizability for the molecular polariton takes the following form following Eq. (10):

$$\alpha_{e_3ct}=\sum_{i}^{N}P_i\mu_{ri,ct}U_{ie_3}^{\dagger}\left(\frac{1}{\omega_i-\omega_{ct}}+\frac{1}{\omega_i-\omega_{e_3}}\right), \quad (24)$$

where $\mu_{ri,ct}$ denotes the transition dipole between the near-edge state and the charge transfer state. For this system, we

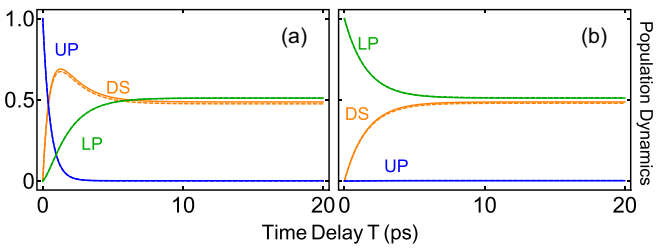

FIG. 11. Comparison of the population resolved by the signal (dashed line) with the population obtained from the master equation (solid line), for $\omega - v = -1.25g$.

have obtained the 2D-FSRS signal with CTs as follows:

$$S_{ct}(\omega_0,\omega-\omega_2,T)=\frac{1}{\pi}\mathrm{Im}(-i)^3\varepsilon_3^*(\omega)\int_0^\infty dt\int_0^t d\tau\sum_{e_1e_2e_3e_4}^{N+1}\mu_{ge_1}\mu_{ge_2}\alpha_{e_3ct}\alpha_{cte_4}\left(\frac{1}{-\omega_0-\xi_{ge_1}}+\frac{1}{\omega_0-\xi_{e_1g}}\right)$$
$$\times\,\varepsilon_2(t-T)e^{i\omega(t-T)}\varepsilon_2^*(\tau-T)\varepsilon_3(\tau-T)G_{e_4e_3,e_2e_1}(\tau-T_2)e^{-i\omega_{e_4ct}(t-\tau)}. \tag{25}$$

To visualize our signal, we consider 10 molecules and assume that the energy of the charge transfer state is 1.6 eV, as shown in Fig. 12. Since the parametric process is not included in this case, a peak located at $\omega_{e_3e_5}\geqslant 0$ accurately reflects the density matrix ρ_{e_3,e_3}. This fact should be kept in mind when analyzing Fig. 12 and comparing it with the real-time dynamics in Fig. 9. Initially, we consider the pulse pumping to the upper polariton, as shown in the upper part of the signal plots in Fig. 12. The peak $\omega-\omega_2=\omega_{\mathrm{lp,ct}}$ only contains the (a') and (c') processes in Fig. 2 with Raman shift $\omega_{\mathrm{lp,ct}}$. The behavior of the peak at $\omega-\omega_2=\omega_{\mathrm{lp,ct}}=230$THz demonstrates the dynamics of the upper polariton, which continues to grow as indicated by the increasing intensity of the relevant peak. Conversely, the peak at $\omega-\omega_2=\omega_{\mathrm{ds,ct}}=360$THz represents the dynamics of the dark state: the density matrix increases over time and then begins to decay. Last, the peak at $\omega-\omega_2=\omega_{\mathrm{up,ct}}=450$THz reflects the dynamics of the upper polariton, which is indicated by the decreasing peak intensity.

In the lower part of the population depicted in Fig. 12, where the system is initially pumped to the lower polariton, the peak at $\omega-\omega_2=\omega_{\mathrm{up,ct}}$ is absent at all time delays. This absence is due to the energy of the upper polariton being too high to undergo relaxation. The decreasing intensity of the peak at $\omega-\omega_2=\omega_{\mathrm{lp,ct}}$ and the increasing intensity of the peak at $\omega-\omega_2=\omega_{\mathrm{ds,ct}}$ correspond to the decay of the UP state and the growth of the dark state, respectively.

In the coherence part of Fig. 12, we observe that peaks predominantly appear around $\omega-\omega_2=\omega_{\mathrm{lp,ct}}$ and $\omega-\omega_2=\omega_{\mathrm{up,ct}}$. This predominance is due to the selection rule that forbids initial pumping to the dark states. As is typical, the peaks exhibit an oscillatory decay. Moreover, we can clearly observe the oscillation at the peak, transitioning from "all red," through "half red, half blue," to "all blue." The fading color also indicates that the oscillation is decaying. Regarding the total signal, it is important to note that the "red dot" (positive part) in Fig. 12(b) consistently represents the contribution of the population, as the positive and negative values of coherence are identical. It is evident that Figs. 12(c) and 12(d) are identical to the pure population, implying that the coherence has dissipated.

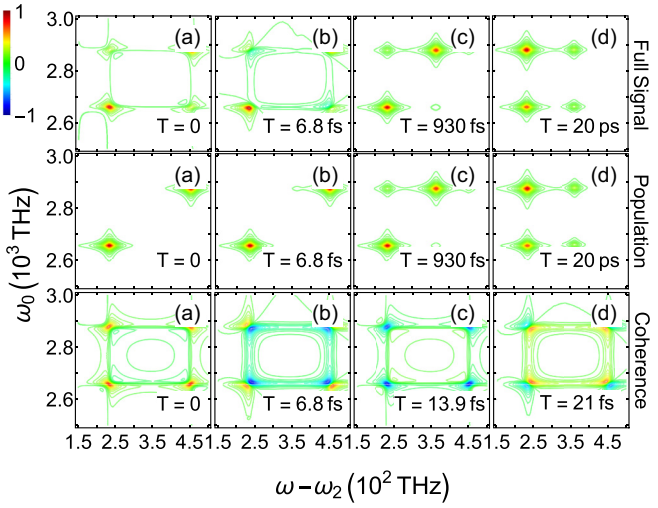

FIG. 12. FSRS signal with detuning $\omega-v=1.25g$. The energy of the charge transfer state is 1.6 eV.

VII. CONCLUSION AND REMARKS

We studied the coherent Raman response of molecular polaritons, in which the dark states are visualized. The results led to 2D FSRS for cavity-polariton systems, and we therefore proposed a microscopic theory for the FSRS signal. Rich information about the dark-state polaritons and their coupling to the bright polaritons can be readily visualized in the 2D FSRS. Our work provides an off-resonant spectroscopic scheme for real-time monitoring of dark-state-polariton dynamics, not accessible by conventional spectroscopic techniques, including absorption and fluorescence. The multidimensional projections of the FSRS signal, as elaborated, enable a multiscale illustration of the polariton dynamics in crosstalk with the DPSs, underlying a time- and frequency-resolved nature.

Our work would be insightful for the study of polariton-afforded reactivity of photoactive molecules and cavity-coupled heterostructures, including 2D semiconductors. The FSRS in the present work can enable a clean fingerprint for the fast nonadiabatic electron dynamics, where complex energy potentials involving anharmonicity need to be taken into account. These would be a remarkable generalization of our present work and will be presented elsewhere.

ACKNOWLEDGMENTS

J.R. and Z.Z. gratefully acknowledge the support of the Early Career Scheme from the Hong Kong Research Grants Council (No. 21302721), the National Science Foundation of China (No. 12104380), the National Science Foundation of China/RGC Collaborative Research Scheme (No. CRS-CUHK401/22 for Research Projects-RMGS (No. 9229137), and ARPC-CityU New Research Initiative/Infrastructure Support from Central (No. 9610505).

[1] J. Fregoni, F. J. Garcia-Vidal, and J. Feist, Theoretical challenges in polaritonic chemistry, ACS Photonics **9**, 1096 (2022).

[2] S. Kena-Cohen and S. R. Forrest, Room-temperature polariton lasing in an organic single-crystal microcavity, Nat. Photonics **4**, 371 (2010).

[3] T. Cookson, K. Georgiou, A. Zasedatelev, R. T. Grant, T. Virgili, M. Cavazzini, F. Galeotti, C. Clark, N. G. Berloff, D. G. Lidzey, and P. G. Lagoudakis, A yellow polariton condensate in a dye filled microcavity, Adv. Opt. Mater. **5**, 1700203 (2017).

[4] J. D. Plumhof, T. Stoferle, L. Mai, U. Scherf, and R. F. Mahrt, Room-temperature Bose-Einstein condensation of cavity exciton-polaritons in a polymer, Nat. Mater. **13**, 247 (2014).

[5] J. A. Hutchison, T. Schwartz, C. Genet, E. Devaux, and T. W. Ebbesen, Modifying chemical landscapes by coupling to vacuum fields, Angew. Chem. **124**, 1624 (2012).

[6] A. Thomas, J. George, A. Shalabney, M. Dryzhakov, S. J. Varma, J. Moran, T. Chervy, X. Zhong, E. Devaux, C. Genet *et al.*, Ground-state chemical reactivity under vibrational coupling to the vacuum electromagnetic field, Angew. Chem. Int. Ed. **55**, 11462 (2016).

[7] X. Zhong, T. Chervy, S. Wang, J. George, A. Thomas, J. A. Hutchison, E. Devaux, C. Genet, and T. W. Ebbesen, Nonradiative energy transfer mediated by hybrid light-matter states, Angew. Chem. Int. Ed. **55**, 6202 (2016).

[8] D. M. Coles, N. Somaschi, P. Michetti, C. Clark, P. G. Lagoudakis, P. G. Savvidis, and D. G. Lidzey, Polariton-mediated energy transfer between organic dyes in a strongly coupled optical microcavity, Nat. Mater. **13**, 712 (2014).

[9] C. Schäfer, M. Ruggenthaler, H. Appel, and A. Rubio, Modification of excitation and charge transfer in cavity quantum-electrodynamical chemistry, Proc. Natl. Acad. Sci. USA **116**, 4883 (2019).

[10] D. Hagenmüller, S. Schütz, J. Schachenmayer, C. Genes, and G. Pupillo, Cavity-assisted mesoscopic transport of fermions: Coherent and dissipative dynamics, Phys. Rev. B **97**, 205303 (2018).

[11] D. Hagenmüller, J. Schachenmayer, S. Schütz, C. Genes, and G. Pupillo, Cavity-enhanced transport of charge, Phys. Rev. Lett. **119**, 223601 (2017).

[12] E. Orgiu, J. George, J. A. Hutchison, E. Devaux, J. F. Dayen, B. Doudin, F. Stellacci, C. Genet, J. Schachenmayer, C. Genes, G. Pupillo, P. Samorì, and T. W. Ebbesen, Conductivity in organic semiconductors hybridized with the vacuum field, Nat. Mater. **14**, 1123 (2015).

[13] B. Xiang, R. F. Ribeiro, L. Chen, J. Wang, M. Du, J. Yuen-Zhou, and W. Xiong, State-selective polariton to dark state relaxation dynamics, J. Phys. Chem. A **123**, 5918 (2019).

[14] A. B. Grafton, A. D. Dunkelberger, B. S. Simpkins, J. F. Triana, F. J. Hernández, F. Herrera, and J. C. Owrutsky, Excited-state vibration-polariton transitions and dynamics in nitroprusside, Nat. Commun. **12**, 214 (2021).

[15] M. Kowalewski, J. Mikosch, R. Wester, and R. de Vivie-Riedle, Nucleophilic substitution dynamics: Comparing wave packet calculations with experiment, J. Phys. Chem. A **118**, 4661 (2014).

[16] M. Du and J. Yuen-Zhou, Catalysis by dark states in vibropolaritonic chemistry, Phys. Rev. Lett. **128**, 096001 (2022).

[17] Z. Zhang, S. Zhao, and D. Lei, Quantum statistical theory for an exciton-polariton condensate: Fluctuations and coherence, Phys. Rev. B **106**, L220306 (2022).

[18] R. F. Ribeiro, L. A. Martínez-Martínez, M. Du, J. Campos-Gonzalez-Angulo, and J. Yuen-Zhou, Polariton chemistry: Controlling molecular dynamics with optical cavities, Chem. Sci. **9**, 6325 (2018).

[19] B. Xiang and W. Xiong, Molecular vibrational polariton: Its dynamics and potentials in novel chemistry and quantum technology, J. Chem. Phys. **155**, 050901 (2021).

[20] Z. Zhang, K. Wang, Z. Yi, M. S. Zubairy, M. O. Scully, and S. Mukamel, Polariton-assisted cooperativity of molecules in microcavities monitored by two-dimensional infrared spectroscop, J. Phys. Chem. Lett. **10**, 4448 (2019).

[21] B. Xiang, R. F. Ribeiro, A. D. Dunkelberger, and W. Xiong, Two-dimensional infrared spectroscopy of vibrational polaritons, Proc. Natl. Acad. Sci. USA **115**, 4845 (2018).

[22] S. Cordero, O. Castaños, R. López-Peña, and E. Nahmad-Achar, Effect of the atomic dipole-dipole interaction on the phase diagrams of field-matter interactions: Variational procedure, Phys. Rev. A **105**, 033712 (2022).

[23] F. Herrera and C. S. Frank, Theory of nanoscale organic cavities: The essential role of vibration-photon dressed states, ACS Photonics **5**, 65 (2018) 2408.

[24] A. S. Davydov, *Theory of Molecular Excitons* (Plenum, New York, 1971).

[25] F. C. Spano, J. R. Kuklinski, and S. Mukamel, Cooperative radiative dynamics in molecular aggregates, J. Chem. Phys. **94**, 7534 (1991).

[26] D. Abramavicius, B. Palmieri, D. V. Voronine, F. Šanda, and S. Mukamel, Coherent multidimensional optical spectroscopy of excitons in molecular aggregates; quasiparticle versus supermolecule perspectives, Chem. Rev. **109**, 2350 (2009),.

[27] V. I. Novoderezhkin, M. A. Palacios, H. Van Amerongen, and R. Van Grondelle, Energy-transfer dynamics in the LHCII complex of higher plants: Modified Redfield approach, J. Phys. Chem. B **108**, 10363 (2004).

[28] D. W. McCamant, P. Kukura, and R. A. Mathies, Femtosecond time-resolved stimulated Raman spectroscopy:Application to the ultrafast internal conversion in β-carotene, J. Phys. Chem. A **107**, 8208 (2003).

[29] S.-Y. Lee, D. Zhang, D. W. McCamant, P. Kukura, and R. A. Mathies, Theory of femtosecond stimulated Raman spectroscopy, J. Chem. Phys. **121**, 3632 (2004).

[30] P. Kukura, D. W. McCamant, S. Yoon, D. B. Wandschneider, and R. A. Mathies, Structural observation of the primary isomerization in vision with femtosecond-stimulated Raman, Science **310**, 1006 (2005).

[31] P. Kukura, D. W. McCamant, and R. A. Mathies, Femtosecond stimulated Raman spectroscopy, Annu. Rev. Phys. Chem. **58**, 461 (2007).

[32] H. Kuramochi, S. Takeuchi, and T. Tahara, Ultrafast structural evolution of photoactive yellow protein chromophore revealed by ultraviolet resonance femtosecond stimulated Raman spectroscopy, J. Phys. Chem. Lett. **3**, 2025 (2012).

[33] D. R. Dietze and R. A. Mathies, Femtosecond stimulated Raman spectroscopy, ChemPhysChem **17**, 1224 (2016).

[34] G. Batignani, C. Ferrante, and T. Scopigno, Accessing excited state molecular vibrations by femtosecond stimulated Raman spectroscopy, J. Phys. Chem. Lett. **11**, 7805 (2020).

[35] C. Ferrante, G. Batignani, E. Pontecorvo, L. C. Montemiglio, M. H. Vos, and T. Scopigno, Ultrafast dynamics and vibrational relaxation in six-coordinate heme proteins revealed by fem-

tosecond stimulated Raman spectroscopy, J. Am. Chem. Soc. **142**, 2285 (2020).

[36] P. G. Lynch, A. Das, S. Alam, C. C. Rich, and R. R. Frontiera, Mastering femtosecond stimulated Raman spectroscopy: A practical guide, ACS Phys. Chem Au **4**, 1 (2023).

[37] Z. Zhang, T. Peng, X. Nie, G. S. Agarwal, and M. O. Scully, Entangled photons enabled time-frequency-resolved coherent Raman spectroscopy and applications to electronic coherences at femtosecond scale, Light Sci. Appl. **11**, 274 (2022).

[38] C. Zhang, M. Gruebele, D. E. Logan, and P. G. Wolynes, Surface crossing and energy flow in many-dimensional quantum systems, Proc. Natl. Acad. Sci. USA **120**, e2221690120 (2023).

[39] K. E. Dorfman, B. P. Fingerhut, and S. Mukamel, Time-resolved broadband Raman spectroscopies: A unified six-wave-mixing representation, J. Chem. Phys. **139**, 124113 (2013).

[40] C. A. Marx, U. Harbola, and S. Mukamel, Nonlinear optical spectroscopy of single, few, and many molecules: Nonequilibrium Green's function QED approach, Phys. Rev. A **77**, 022110 (2008).

[41] P. A. Hobson, W. L. Barnes, D. G. Lidzey, G. A. Gehring, D. M. Whittaker, M. S. Skolnick, S. Walker, Strong excitonphoton coupling in a low-Q all-metal mirror microcavity, Appl. Phys. Lett. **81**, 3519 (2002).

[42] Z. Zhang, X. Nie, D. Lei, and S. Mukamel, Multidimensional coherent spectroscopy of molecular polaritons: Langevin approach, Phys. Rev. Lett. **130**, 103001 (2023).

[43] A. Tokmakoff, M. J. Lang, D. S. Larsen, G. R. Fleming, V. Chernyak, and S. Mukamel, Two-dimensional Raman spectroscopy of vibrational interactions in liquids, Phys. Rev. Lett. **79**, 2702 (1997).

[44] G. Fumero, C. Schnedermann, G. Batignani, T. Wende, M. Liebel, G. Bassolino, C. Ferrante, S. Mukamel, P. Kukura, and T. Scopigno, Two-dimensional impulsively stimulated resonant Raman spectroscopy of molecular excited states, Phys. Rev. X **10**, 011051 (2020).

[45] Y. J. Yan and S. Mukamel, Femtosecond pump-probe spectroscopy of polyatomic molecules in condensed phases, Phys. Rev. A **41**, 6485 (1990).

[46] F. Fassioli, K. H. Park, S. E. Bard, and G. D. Scholes, Femtosecond photophysics of molecular polaritons, J. Phys. Chem. Lett. **12**, 11444 (2021).